Nanoelectronics and Its New Materials – A NEW ERA OF NANOSCIENCE

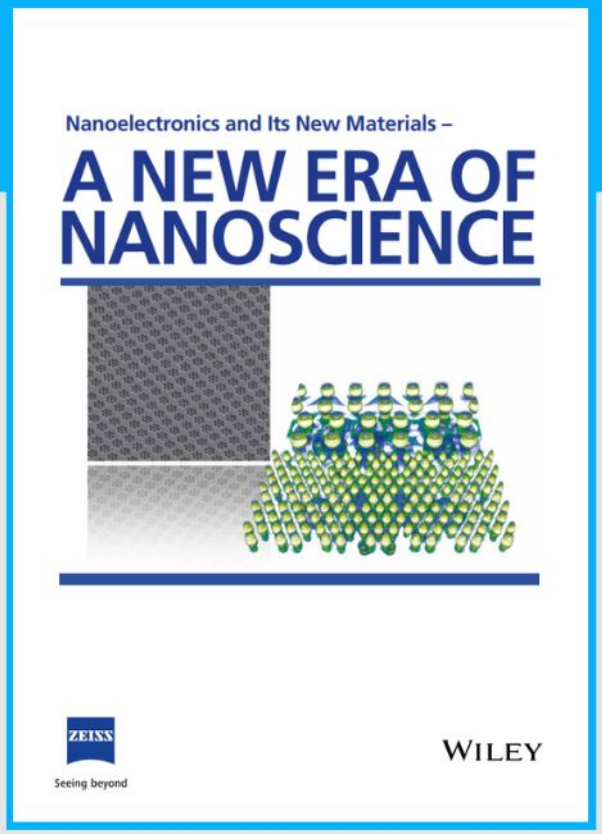

Discover the recent advances in electronics research and fundamental nanoscience.

Nanotechnology has become the driving force behind breakthroughs in engineering, materials science, physics, chemistry, and biological sciences. In this compendium, we delve into a wide range of novel applications that highlight recent advances in electronics research and fundamental nanoscience. From surface analysis and defect detection to tailored optical functionality and transparent nanowire electrodes, this eBook covers key topics that will revolutionize the future of electronics.

To get your hands on this valuable resource and unleash the power of nanotechnology, simply download the eBook now. Stay ahead of the curve and embrace the future of electronics with nanoscience as your guide.

ZEISS

Seeing beyond

WILEY

Check for updates

NANO · MICRO small
www.small-journal.com

High Selectivity and Sensitivity in Chemiresistive Sensing of Co(II) Ions with Liquid-Phase Exfoliated Functionalized MoS_2: A Supramolecular Approach

Anna Zhuravlova, Antonio Gaetano Ricciardulli, Dawid Pakulski, Adam Gorczyński, Adam Kelly, Jonathan N. Coleman, Artur Ciesielski,* and Paolo Samorì**

Chemical sensing of water contamination by heavy metal ions is key as it represents a most severe environmental problem. Liquid-phase exfoliated two-dimensional (2D) transition metal dichalcogenides (TMDs) are suitable candidates for chemical sensing thanks to their high surface-to-volume ratio, sensitivity, unique electrical characteristics, and scalability. However, TMDs lack selectivity due to nonspecific analyte-nanosheet interactions. To overcome this drawback, defect engineering enables controlled functionalization of 2D TMDs. Here, ultrasensitive and selective sensors of cobalt(II) ions via the covalent functionalization of defect-rich MoS_2 flakes with a specific receptor, 2,2′:6′,2″-terpyridine-4′-thiol is developed. A continuous network is assembled by healing of MoS_2 sulfur vacancies in a tailored microfluidic approach, enabling high control over the assembly of thin and large hybrid films. The Co^{2+} cations complexation represents a powerful gauge for low concentrations of cationic species which can be best monitored in a chemiresisitive ion sensor, featuring a 1 pM limit of detection, sensing in a broad concentration range (1 pM – 1 µM) and sensitivity as high as 0.308 ± 0.010 $lg([Co^{2+}])^{-1}$ combined with a high selectivity towards Co^{2+} over K^+, Ca^{2+}, Mn^{2+}, Cu^{2+}, Cr^{3+}, and Fe^{3+} cations. This supramolecular approach based on highly specific recognition can be adapted for sensing other analytes through specific ad-hoc receptors.

1. Introduction

The relentless escalation of industrial and agricultural activities due to population growth for decades has resulted in a dramatic increase in pollutants released into the environment worldwide.[1] These contaminants, which are chemically very diverse and range from micropollutants[2] and distillates[3] to heavy metals[4] and endocrine disruptors,[5] represent one of the biggest threat for the world's population. Therefore, the development of new robust chemical sensors allowing the monitoring of the water composition in an efficient and rapid manner is highly sought after. The toxicity of heavy metals (e.g., Hg^{2+}, Cd^{2+}, Pb^{2+}, Cu^{2+}, Co^{2+}, Cr^{3+}, Mn^{2+}, etc.) arises from their water-soluble nature along with their nonbiodegradability, prolonged half-life and potential of accumulation in different parts of living organisms including cells, tissues, and organs, even upon moderate exposure.[4] To address such environmental challenges, it is

A. Zhuravlova, A. G. Ricciardulli, A. Ciesielski, Prof. P. Samorì
Université de Strasbourg
CNRS
ISIS
8 allée Gaspard Monge, Strasbourg 67000, France
E-mail: ricciardulli@unistra.fr; ciesielski@unistra.fr; samori@unistra.fr
D. Pakulski
Adam Mickiewicz University Foundation
Poznań Science and Technology Park
Rubież 46, Poznań 61-612, Poland

The ORCID identification number(s) for the author(s) of this article can be found under https://doi.org/10.1002/smll.202208100.

© 2023 The Authors. Small published by Wiley-VCH GmbH. This is an open access article under the terms of the Creative Commons Attribution License, which permits use, distribution and reproduction in any medium, provided the original work is properly cited.

DOI: 10.1002/smll.202208100

D. Pakulski, A. Ciesielski
Centre for Advanced Technologies
Adam Mickiewicz University
Uniwersytetu Poznańskiego 10, Poznań 61–614, Poland
A. Gorczyński
Faculty of Chemistry
Adam Mickiewicz University in Poznan
Uniwersytetu Poznanskiego 8, Poznan 61–614, Poland
Dr. A. Kelly, Prof. J. N. Coleman
School of Physics
Centre for Research on Adaptive Nanostructures and Nanodevices (CRANN) and Advanced Materials and Bioengineering Research (AMBER)
Trinity College Dublin
Dublin Dublin 2, Ireland

critical to develop a facile, cheap, and robust technology for sensing metal cations in water reservoirs, such as lakes and ponds, as well as in waterbodies, namely rivers, and seas. The detection of heavy metal ions at low concentrations, i.e., in the picomolar regime, requires the use of analytical methods including spectroscopic techniques, such as ion chromatography and ultraviolet–visible spectroscopy,[6] atomic flame atomic absorption spectroscopy,[7] inductively coupled plasma-mass spectrometry,[8] atomic emission spectrometry,[9] capillary electrophoresis,[10] X-ray fluorescence spectroscopy,[11] and microprobes.[12] Although these analytical methods are highly sensitive and selective, they require expensive instruments, preconcentration procedures, and professional personnel. Furthermore, they cannot be used as portable devices for on-site detection because of larger size of the equipment. On the other hand, chemical sensors have been widely applied for on-site detection of multiple heavy metals. In particular, nanomaterials-based sensors have shown great promise in the detection of heavy metals due to their large surface area, high catalytic efficiency, high surface reactivity, and strong adsorption capacity.[13] Moreover, they meet the current request for portable multifunctional devices with an electrical response and can be easily integrated into miniaturized devices[14] and sensor arrays[15] for lab-on-a-chip applications. Among different nanomaterials, metallic nanoparticles (NPs) have been extensively exploited for metals sensing in biological liquids and drinking water mostly thanks to their plasmonic properties.[16] However, NPs and their colloidal dispersions suffer from severe aggregation and usually require capping agents to enhance their stability.[17] Additionally, the properties of the NPs are strongly dependent on their shape, resulting in uneven electrical properties. The aforementioned drawbacks can be overcome by employing two-dimensional materials (2DMs) as platforms for chemical sensing. 2DMs offer high mechanical robustness, unique electronic properties, such as high electron mobilities, and ease of processability, making them the platform of choice for proof-of-concept portable sensors with electrical readout.[18–20] Indeed, 2D nanosheets have been used for the detection of a wide variety of inorganic and (bio)organic analytes, through their integration into diverse sensing devices, including thin film transistors and chemiresistors.[13,18,21] Additionally, nanosheet-based devices benefit from low power consumption[22] and good nanostructure-electrode contact in the case of electrical chemosensors.[13] Moreover, 2DMs can be easily synthesized by top-down exfoliation approaches that yield high quantity, stable and processable dispersions.[23] Hitherto, due to its simple preparation and processing, (reduced) graphene oxide (rGO) has been widely investigated for chemical sensing, both in its pristine form and when chemically functionalized.[13] Yet, the presence of various oxygen-containing groups on their surface determines the existence of numerous uncontrolled background dipole-dipole interactions between GO and charged species, jeopardizing the selectivity in the analyte recognition process. Conversely, less attention has been paid to 2D transition metal dichalcogenides (TMDs) for multireadout sensing of a wide library of analytes.[24] In its pristine form, molybdenum disulfide (MoS_2) has been employed for the sensing of heavy metals, such as mercury (II) cations,[24] and polycyclic aromatic hydrocarbons,[25] in devices with electrical readout. Indeed, the semiconducting nature of MoS_2 makes it susceptible to subtle electronic variations during the sensing process, resulting from doping effect induced by the interaction with analytes. Nevertheless, pristine 2DMs suffer from limited intrinsic selectivity[26] as the analyte-nanosheet interaction occurs through nonspecific physisorption, which is mainly driven by electrostatic and van der Waals forces.[13,27] To overcome this problem, MoS_2 has been functionalized with *ad hoc* receptors for specific analytes via direct basal plane grafting of aryl diazonium salts.[28] However, a general strategy to build solution-processed sensing systems based on TMDs with enhanced sensitivity and selectivity is still missing. In general, structural defects in TMDs nanosheets are considered as a major drawback since they significantly lower the electrical performances of pristine 2D nanosheets.[29] Nonetheless, chalcogen vacancies possess high reactivity and can enable the tuning of MoS_2 physicochemical properties via covalent functionalization with organic supramolecular receptors designed to interact with specific analytes.[30,31] Furthermore, this approach can be implemented to solution-processable TMD inks,[32] enabling scalable production and high compatibility with printing technologies. In general, slow progress in the field of chemical sensing with liquid-phase exfoliated TMDs can be associated with the processability issues. The well-established deposition techniques used with TMDs inks include spray-coating, spin-coating, drop-casting, dry transfer, and inkjet printing, to name a few. Noteworthy, the films prepared by exploiting these techniques do not exhibit thin and even morphologies, limiting the receptor-to-flake ratio in hybrid sensing films, thus severely hindering their sensitivity. Therefore, to fully exploit the defects in TMDs, mostly located at the edges,[32] the implementation of a deposition strategy able to maximize the number of nanosheets for further functionalization via defect engineering is needed.

In this work, we develop ultrasensitive chemical sensors for the detection of heavy metal ions through the covalent functionalization of solution-processed MoS_2 yielding continuous networks. To obtain large and thin hybrid films, we employed for the first time a microfluidic-based deposition approach which allows generation of uniform MoS_2 networks thanks to a controllable laminar flow of liquid-phase exfoliated MoS_2 inks. As a proof of concept, we have decorated defect-rich, liquid phase exfoliated MoS_2 nanosheets with 2,2″:6″,2″-terpyridine-4′-thiol (TerpySH) ligands, whose thiol functional group guarantees their attachment to MoS_2 via the healing of sulfur vacancies. Terpy derivatives are highly selective towards Co^{2+},[33] which is a toxic water pollutant and can cause severe health conditions, such as contact dermatitis, allergic asthma, and lung cancer upon overexposure.[34] The fabricated chemiresisitive ion sensors exhibit a state-of-the-art limit of detection (LoD) reaching values as low as 1 pM (0.06 ng L^{-1}) of Co^{2+}, sensing within a broad concentration range from 1 pM to 1 μM and high selectivity towards Co^{2+} cation over interfering species such as K^+, Ca^{2+}, Fe^{3+}, Cu^{2+}, Cr^{3+}, and Mn^{2+}. Our strategy can be extended to other 2D materials and finely tuned supramolecular receptor combinations, paving the way for the versatile design of highly selective chemical sensors with tailored functionalities and electrical readout.

© 2023 The Authors. Small published by Wiley-VCH GmbH

16136829, 0, Downloaded from https://onlinelibrary.wiley.com/doi/10.1002/smll.202208100 by Library Of Trinity College, Wiley Online Library on [03/10/2023]. See the Terms and Conditions (https://onlinelibrary.wiley.com/terms-and-conditions) on Wiley Online Library for rules of use; OA articles are governed by the applicable Creative Commons License

2. Results and Discussion

The functionalized solution-processed MoS_2 films onto Si/SiO_2 support prepatterned with interdigitated Au electrodes (channel width of 10 μm) (Figure S1, Supporting Information) were formed by means of a step-by-step deposition process that involves a microfluid strategy to finely control the laminar flow of the MoS_2 ink and thus generating a large and thin MoS_2 coating. First, the Si/SiO_2 substrate was modified with 3-(aminopropyl)triethoxysilane (APTES) to adjust its wettability, thereby promoting the adhesion of 2DMs nanosheets. The film formation was carried out inside a microfluidic chamber (Figure S2, Supporting Information) by repeating the subsequent deposition of liquid-phase exfoliated MoS_2 from its ink in isopropanol followed by the covalent functionalization of the nanosheets edges with $[Zn(TerpySH)_2](OTf)_2$ in chloroform/acetonitrile 4:1 *v/v* yielding three-dimensional networks of MoS_2 bridged by highly selective supramolecular receptors for Co^{2+} cations (**Figure 1**a,b). As a result, films exhibiting ≈60% coverage were generated (Figure S3, Supporting Information). It is worth noting that exfoliation of bulk MoS_2 by sonication-assisted methods yields a considerable amount of structural defects in the synthesized flakes, such as sulfur vacancies,[30,32] which are critical to the assembly of a robust network as they are exploited as anchoring sites for the thiolated terpyridine moieties. To impart sensitivity towards Co^{2+} ions, MoS_2-$[Zn(TerpySH)_2]^{2+}$ films were treated with 1 mM HCl, which enables the removal of Zn^{2+} ions from the $[Zn(TerpySH)_2]^{2+}$ units via its decomplexation,[35] giving rise to coordination pockets that can be further exploited for the complexation of Co^{2+} cations. Noteworthy, the morphology of MoS_2-TerpySH hybrid films remains unchanged upon the treatment with HCl, which is critical in view of recyclability.

The composition and structural features of the thin films were assessed by scanning electron microscopy (SEM), X-ray photoelectron spectroscopy (XPS), and Raman spectroscopy. The comparison of SEM images (Figure 1c,d) of the pristine MoS_2 film and the ones of the networks thereof obtained via the treatment with the dithiolated ligands demonstrates higher coverage for the latter. This result suggests that the dithiolated molecules act as a linker thereby bridging adjacent flakes, yielding a covalent network. XPS is a powerful technique to unveil the defects type and content in MoS_2 (Figure S4, Supporting Information). The high-resolution spectra of the S2p peak for the pristine and complex-functionalized film (Figure 1e,f) feature two main sulfur peaks at ≈162.3 and ≈163.5 eV, which are ascribed to the $S2p_{3/2}$ and $S2p_{1/2}$ components, respectively, and a broad component at ≈161.2 eV that emerges from the defects of crystal structure.[24,25,32] The decrease of the relative area of the defect peak from 8.7% in the pristine film to 6.7% in complex-treated one bears witness to the efficient defect healing and thus chemical functionalization of MoS_2 nanosheets. Additionally, XPS provided evidence for the complete Zn(II) ion removal upon HCl treatment (Figures S5 and S6, Supporting Information). The Raman spectra of MoS_2 of pristine and functionalized films (Figure 1g) feature the E^1_{2g} at ≈381 cm^{-1} and A_{1g} at ≈407 cm^{-1} vibrational signature, ascribed to in-plane and out-of-plane modes, respectively.[36] Raman analysis revealed identical spectral features indicating that the functionalization procedure does not damage or modify the flakes and their orientation. Indeed, the full width half maximum (FWHM) of both peaks displays no significant change (from 4.93 ± 0.19 cm^{-1} to 5.12 ± 0.17 cm^{-1} for E^1_{2g} and from 4.43 ± 0.23 cm^{-1} to 4.73 ± 0.21 cm^{-1} for A_{1g}). Both components also exhibit a blue shift of ≈1.5 cm^{-1}, which confirms the successful functionalization process.[32]

To unravel the sensing performances of the MoS_2-TerpySH network, electrochemical impedance spectroscopy (EIS) measurements were performed. This technique is based on alternating current (AC) and it is more sensitive to minor changes in the interface than its direct current counterpart.[37] An interdigitated electrodes design was used to overcome the negative effects of film coverage disruptions and enhance the active sensing area (**Figure 2**a and S1a).[38] Ultimately, our system was modeled by an equivalent circuit, as shown in the inset of Figure 2c, where R1 represents the MoS_2-gold contact resistance, R2, and CPE1 are attributed to the charge transfer resistance (R_{ct}) of the film, and its double-layer capacitance, respectively, and R3 and CPE2 correspond to the resistance and capacitance of a diffusion boundary layer in bulk solution.[39] In general, R_{ct} of a thin 2DMs film is governed by the interplay of electronic inter- and intra-flake charge transfer[32] and the ionic conductivity of the solution.[40] The sensing mechanism of the MoS_2-TerpySH film relies on the modulation of its R_{ct}, associated with the complexation between Co^{2+} and two neighboring terpyridine units, strongly affecting the inter-flake electron transfer. The incorporation of immobilized cations into the functionalized film structure induces the redistribution of electron density, hindering both intra- (decreasing the *n*-doping effect of Terpy moiety)[41] and inter-flake electron transport. Additionally, an ionic contribution is present due to a high number of free ions in the system,[40] leading to the decrease of R_{ct}. As a result, the resistance of the film evolves as a function of the analyte (Co^{2+}) concentration (Figure 2b). The EIS spectra comparison between the bare device, pristine MoS_2 film, and the MoS_2-TerpySH film after exposure to 10^{-6} M concentration of $CoCl_2$ is displayed in Figure 2c. As expected, the Nyquist plot of the bare device does not feature a semicircle, associated with R_{ct}, because of the limited charge transfer. In contrast, the pristine and MoS_2-TerpySH films exhibit a R_{ct} of 26.8 kOhm and 170 kOhm, respectively. The higher R_{ct} value in MoS_2-TerpySH film confirms that detection of Co^{2+} is successfully achieved through the Terpy-cobalt(II) recognition rather than nonspecific electrostatic interactions.

To gain further insight into the device sensing performances, a comparative analysis of the sensitivity towards Co^{2+} in pristine and functionalized MoS_2 films was carried out (Figure 2d). Remarkably, the device based on functionalized MoS_2 yielded an average Co^{2+} sensitivity of 0.308 ± 0.010 $lg([Co^{2+}])^{-1}$ in the linear range from 10^{-12} M to 10^{-6} M (R^2 = 0.994) with state-of-the-art ultralow LoD in the picomolar regime as compared with previously reported sensors based on electrical readout and other techniques (Tables S1 and S2, Supporting Information). In contrast, the pristine MoS_2 device demonstrated a negligible average sensitivity of 0.007 ± 0.020 $lg([Co^{2+}])^{-1}$. Alternatively, drop-casted sensing films were prepared according to the previously reported MoS_2 functionalization procedure[32] with subsequent 1 mM HCl treatment. The fabricated films

© 2023 The Authors. Small published by Wiley-VCH GmbH

16136829, 0, Downloaded from https://onlinelibrary.wiley.com/doi/10.1002/smll.202208100 by Library Of Trinity College, Wiley Online Library on [03/10/2023]. See the Terms and Conditions (https://onlinelibrary.wiley.com/terms-and-conditions) on Wiley Online Library for rules of use; OA articles are governed by the applicable Creative Commons License

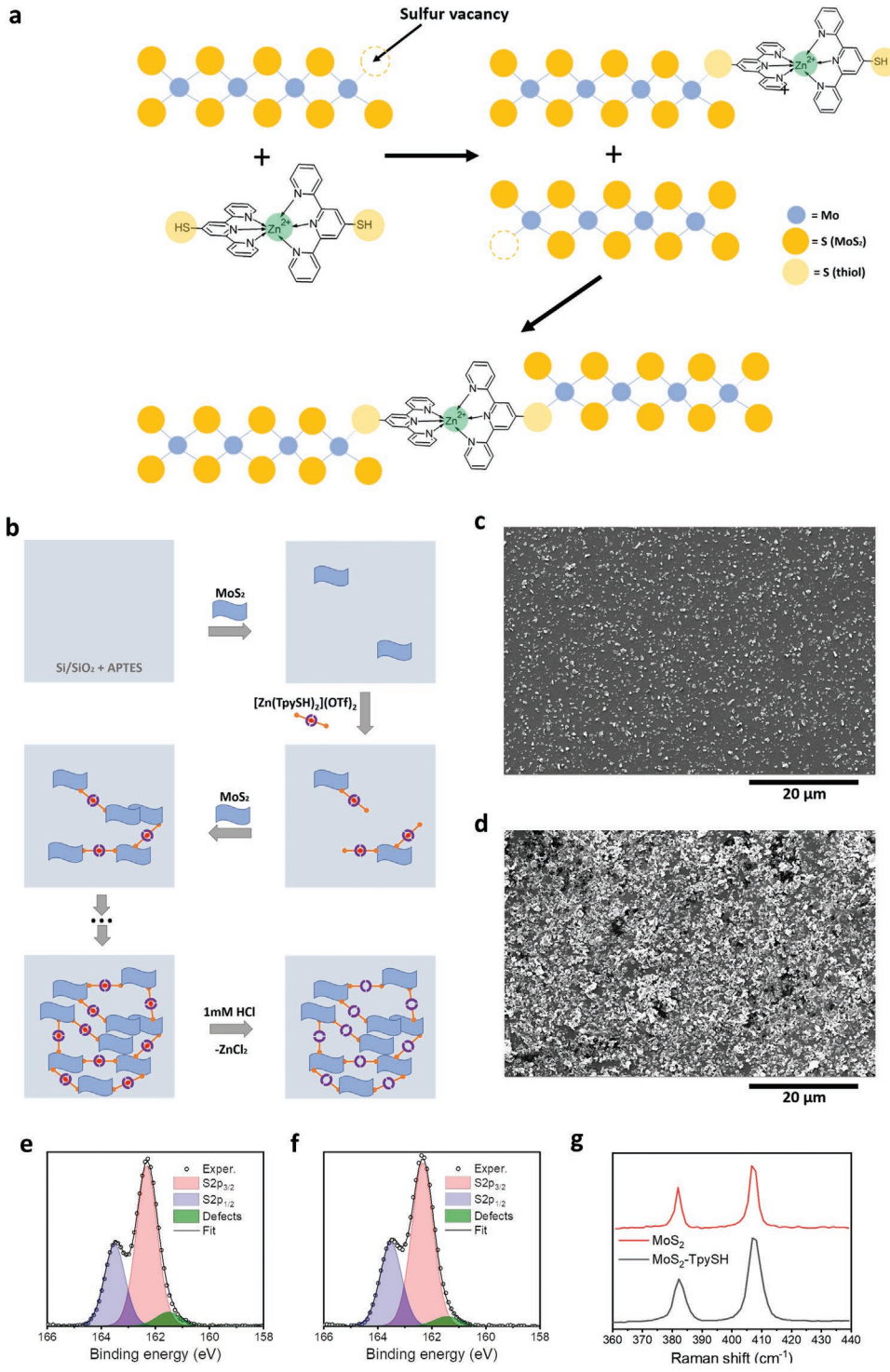

Figure 1. a) Schematic illustration of the healing of sulfur vacancies by thiolated terpyridine complexes. b) Scheme of the step-by-step hybrid film formation. c) SEM image of pristine MoS_2 film fragment. d) SEM image of functionalized MoS_2 film. e) High-resolution XPS spectra of S2p region for pristine and f) functionalized MoS_2. g) Raman spectra of pristine (red) and functionalized (black) MoS_2.

exhibited irregular morphology and the sensitivity to Co^{2+} ion of 0.055 ± 0.012 $lg([Co^{2+}])^{-1}$ with a limit of detection of 10^{-9} M (Figure S7, Supporting Information). Thus, the microfluidic-assisted approach for sensing films assembly provides a significant gain in sensitivity (≈5.6 times) as well as LoD (10^3 times).

To evaluate the selectivity, the response of the film toward potentially interfering cations has been examined. These cations are among the most abundant in tap and wastewater, such as K^+, Ca^{2+}, Cu^{2+}, Cr^{3+}, and Fe^{3+}. To further explore the selectivity of our system, we have investigated its sensing towards Fe^{2+} and

© 2023 The Authors. Small published by Wiley-VCH GmbH

16136829, 0, Downloaded from https://onlinelibrary.wiley.com/doi/10.1002/smll.202208100 by Library Of Trinity College, Wiley Online Library on [03/10/2023]. See the Terms and Conditions (https://onlinelibrary.wiley.com/terms-and-conditions) on Wiley Online Library for rules of use; OA articles are governed by the applicable Creative Commons License

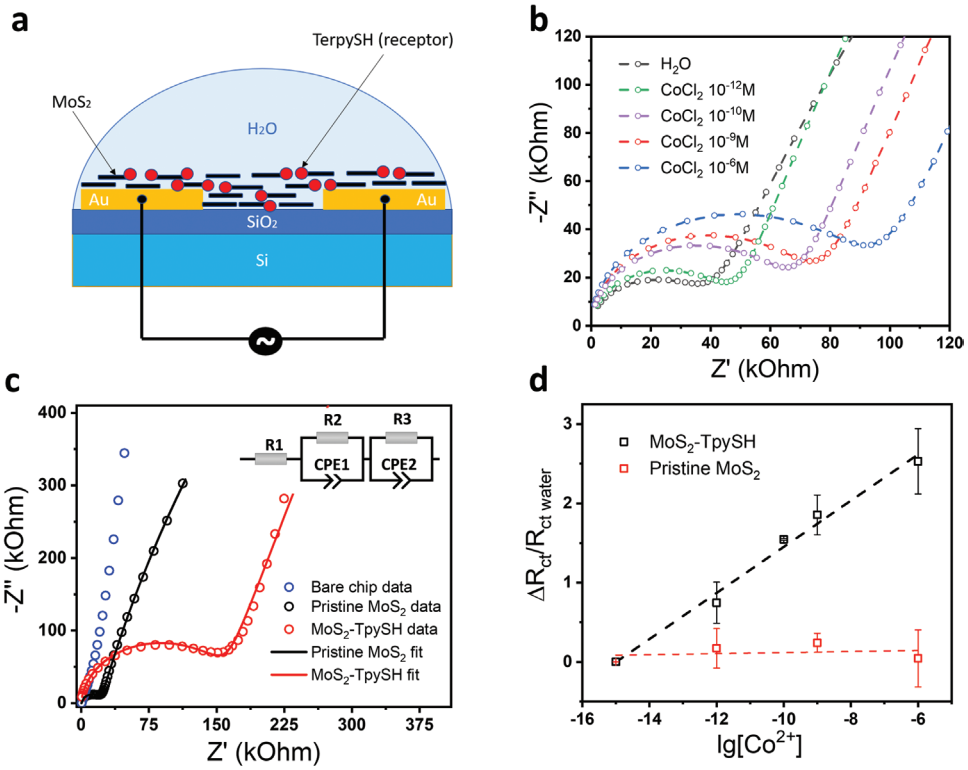

Figure 2. a) Schematic representation of the device architecture. b) EIS signal evolution upon Co^{2+} concentration increase. c) EIS signal variation for bare chip (blue), pristine (black), and functionalized (red) MoS_2 upon exposure of 10^{-6} M solution of $CoCl_2$. Inset: equivalent circuit employed in this study. d) Normalized charge transfer resistance response as a function of $CoCl_2$ concentration for pristine (red) and functionalized (black) device. The slope of calibration curves defines the sensitivity.

Mn^{2+}. Mn^{2+} ion is a neurotoxic heavy metal pollutant[42] comparable in size and coordination number with Co^{2+} (0.080 nm and 0.072 nm for Mn^{2+} and Co^{2+}, respectively).[43] Both Fe^{2+} and Mn^{2+} form bis-complexes with Terpy derivatives.[44,45] It is worth noting that chloride salts were used for all the experiments to exclude the influence of the counter-anion. The comparison of the functionalized film sensitivities towards the Co^{2+}, Mn^{2+}, K^+, Ca^{2+}, Fe^{3+}, Cu^{2+}, Cr^{3+}, and Fe^{2+} cations is shown in **Figure 3**a and Figure S8, Supporting Information. For the Mn^{2+} cation, the average value of sensitivity was 0.147±0.104 $lg([Mn^{2+}])^{-1}$, being two times smaller than that of Co^{2+}, as a result of the lower stability constant of Mn^{2+} bis-complex over Co^{2+}.[45] Large error bars for the device sensitivity towards Mn^{2+} are explained by high device-to-device variation as well as the unstable nature of its bis-complex with the TerpySH ligand. Similarly, the calibration curve for Fe^{2+} is characterized by the positive slope of 0.439 ± 0.034 $lg([Fe^{2+}])^{-1}$. Indeed, Fe^{2+} ion is known to readily form stable bis-complexes with Terpy derivatives with a significantly higher stability constant than that of Co^{2+} ($logK_2 = 9.9$ for Co^{2+} and 13.8 for Fe^{2+}).[45] Although the sensitivity of the sensor to Fe^{2+} is significant, the sensing of Co^{2+} in tap or waste water is not jeopardized because such water undergoes aeration or chlorination prior to use or disposal. As a result, most of the Fe^{2+} is oxidized to insoluble Fe^{3+} compounds.[46]

In contrast, the average sensitivities for K^+ and Cr^{3+} are –0.035 ± 0.031 $lg([K^+])^{-1}$ and –0.069 ± 0.011 $lg([Cr^{3+}])^{-1}$, respectively, which are one order of magnitude lower than that for Co^{2+}. Moreover, the slopes of the calibration curves are negative, suggesting that the resistance of the film decreases proportionally to the ion concentration. Therefore, a different sensing mechanism for K^+ and Cr^{3+} is proposed. As K^+ – Terpy complexes of any stoichiometry are not formed due to the large size (0.141 nm)[43] and coordination number (8) of the metal ion, the interactions involved are merely electrostatic. On the other hand, Cr^{3+} has a smaller ionic radius compared to Co^{2+} (0.058 nm for Cr^{3+}).[43] Thus, K^+ and Cr^{3+} ions are not retained by the ligands to form a complex but are rather mobile within the structure, significantly contributing to the overall ionic conductivity of the film. As expected, Ca^{2+} and Fe^{3+} induced negligible output of the sensor with the sensitivities of 0.003 ± 0.010 $lg([Ca^{2+}])^{-1}$ and 0.007 ± 0.018 $lg([Fe^{3+}])^{-1}$. Indeed, the low-affinity Ca^{2+} and Fe^{3+} to Terpy, explained by the high stability of their oxygen-containing aquacomplexes[47] and unsuitable cation size for Ca^{2+} (0.103 nm)[43] and Fe^{3+} (0.064 nm),[43] respectively, leads to reduced R_{ct} output. The sensor response to Cu^{2+} features the calibration curve slope of 0.063±0.011 $lg([Cu^{2+}])^{-1}$. Such moderate sensitivity for Cu^{2+} is ascribed to the formation of a 1:1 complex with Terpy ligand, due to suitable cation size (0.072 nm)[43] and coordination number 4. Therefore, the neighboring Terpy units are not connected through a cation. Thus, the contribution of interflake transport does not change significantly.

Additionally, to investigate the sensitivity and selectivity of our sensor in a bicomponent system, an experiment of sensing

© 2023 The Authors. Small published by Wiley-VCH GmbH

16136829, 0, Downloaded from https://onlinelibrary.wiley.com/doi/10.1002/smll.202208100 by Library Of Trinity College, Wiley Online Library on [03/10/2023]. See the Terms and Conditions (https://onlinelibrary.wiley.com/terms-and-conditions) on Wiley Online Library for rules of use; OA articles are governed by the applicable Creative Commons License

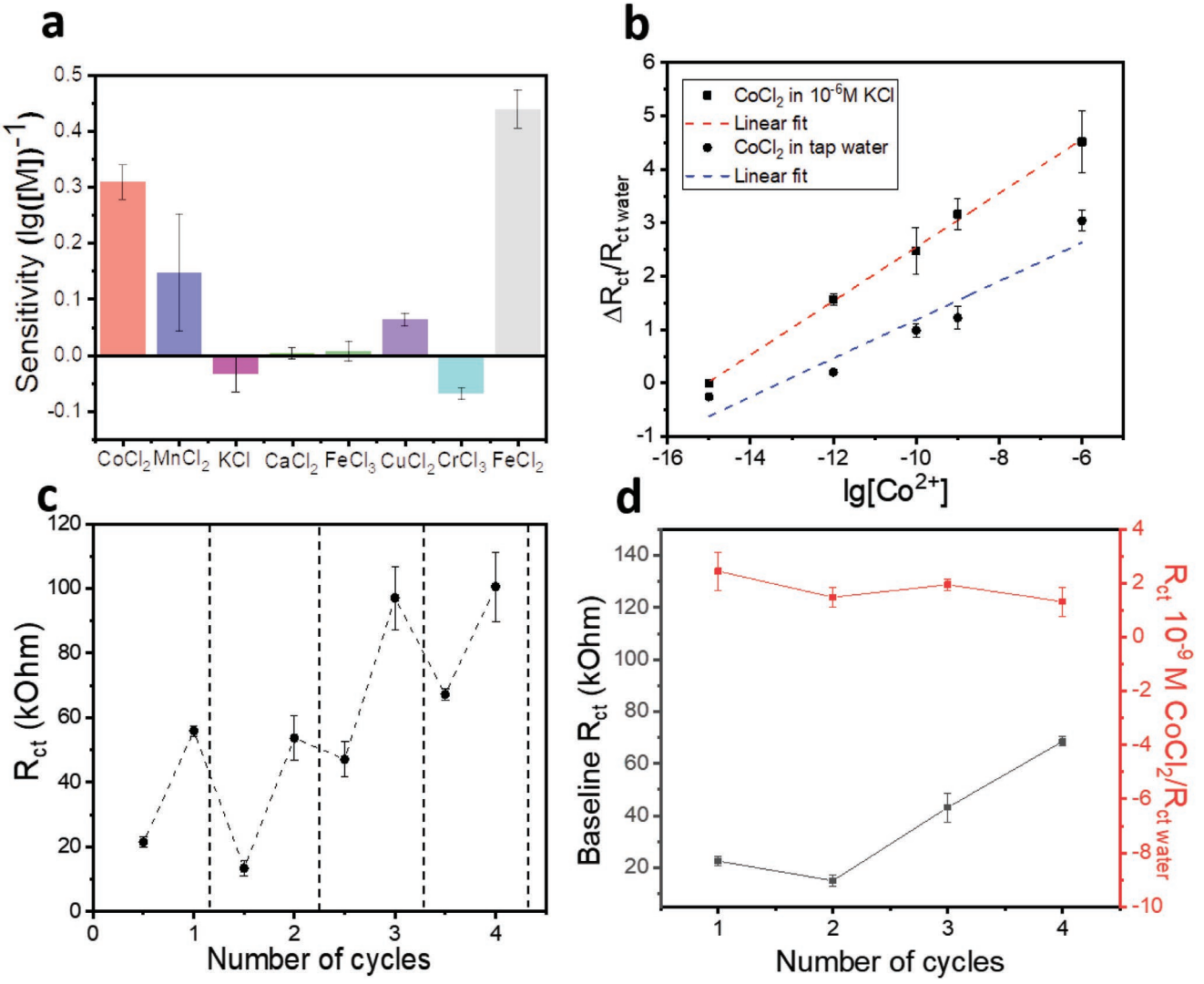

Figure 3. a) Comparison of device sensitivity to the change of concentration for Co^{2+} and interfering cations. [M] is the concentration of a given cation. b) Normalized charge transfer resistance response as a function of $CoCl_2$ concentration with the fixed 10^{-6} M KCl concentration (red) and in tap water (blue). The normalization was performed by the device's R_{ct} in MQ water. c) R_{ct} change as a function of sensing/washing cycles. d) Normalized charge transfer resistance for the detection of Co^{2+} (red) and baseline variation (black) as a function of number of cycles.

Co^{2+} in a 10^{-6} M KCl solution was carried out (Figure 3b). Remarkably, the detection of Co^{2+} was not compromised by the significant excess of another cation in the solution and the average sensitivity increased to 0.453 ± 0.071 lg([Co^{2+}])$^{-1}$. Moreover, to adequately assess the selectivity of the device and its applicability to the real samples, the sensing of Co^{2+} in tap water environment was evaluated. Tap water is a salt-rich matrix that typically contains high concentrations of K^+, Na^+, Ca^{2+}, Cu^{2+}, and traces of other heavy metals.[48] Importantly, the device was able to detect Co^{2+} in a complex multicomponent solution with high sensitivity of 0.361 ± 0.061 lg([Co^{2+}])$^{-1}$, therefore, its selectivity towards Co^{2+} can be concluded. Overall, the results suggest that high selectivity towards a specific analyte or a family of analytes can be achieved through *ad hoc* design of the supramolecular receptor.

To investigate the recyclability of the device, R_{ct} was evaluated after successive $CoCl_2$ treatment/recovery cycles. Since our device operation is governed by reversible supramolecular interactions, the recovery was performed through the decomplexation of the $[Co(TerpySH)_2]^{2+}$ moieties via 10 mM HCl treatment. The R_{ct} change upon repeated 10^{-9} M $CoCl_2$ treatment/recovery is displayed in Figure 3c,d. As shown in Figure 3c, the system can be regenerated up to four times. However, the initial resistance cannot be recovered due to significant baseline drift from 23 to 69 kOhm, resulting from Co^{2+} accumulation and mechanical degradation. Nonetheless, the relative change of R_{ct} is preserved upon multiple Co^{2+} exposure (Figure 3d).

3. Conclusion

In this work, we have developed an unprecedented microfluidic-assisted strategy for selective sensing of heavy metals based on the defect engineering of 2D materials. Sulfur vacancies in

© 2023 The Authors. Small published by Wiley-VCH GmbH

16136829, 0, Downloaded from https://onlinelibrary.wiley.com/doi/10.1002/smll.202208100 by Library Of Trinity College, Wiley Online Library on [03/10/2023]. See the Terms and Conditions (https://onlinelibrary.wiley.com/terms-and-conditions) on Wiley Online Library for rules of use; OA articles are governed by the applicable Creative Commons License

liquid-phase exfoliated MoS_2 have been exploited as anchoring sites for thiolated terpyridine building blocks, enabling the formation thin MoS_2 films. The functionalized MoS_2-TerpySH supramolecular system has been embedded into a chemiresistive sensor for Co^{2+} detection. Our device exhibits superior selectivity towards Co^{2+} over a number of interfering cations including K^+, Cr^{3+}, Cu^{2+}, Ca^{2+}, Mn^{2+}, and Fe^{3+}, with sensitivity as high as 0.308 $lg([Co^{2+}])^{-1}$, the ultralow limit of detection of 1 pM and linearity in the broad range from 1 pM to 1 µM, representing a state-of-the-art chemical sensor compared to best-performing devices based on the electrical readout. Furthermore, the fabricated sensor can be recovered and used multiple (up to 4) times. Our approach can be extended to the detection of a broad range of analytes, spanning from small ions to (bio) organic molecules, by simply tuning the receptor chemical features. Thus, it provides a solid platform for further development of cost-effective and scalable next-generation wearable sensors.

4. Experimental Section

Materials: The materials used to carry out this work are commercially available. MoS_2 powder, hexamethyldisilazane (HMDS), cobalt(II) chloride hexahydrate ($CoCl_2{\times}6H_2O$), calcium chloride dihydrate ($CaCl_2{\times}2H_2O$), iron(III) chloride hexahydrate ($FeCl_3{\times}6H_2O$), manganese(II) chloride tetrahydrate ($MnCl_2{\times}4H_2O$), iron(II) chloride tetrahydrate ($FeCl_2{\times}4H_2O$), chromium(III) chloride hexahydrate ($CrCl_3{\times}6H_2O$), copper(II) chloride dihydrate ($CuCl_2{\times}2H_2O$), precursors for 2,2″:6″,2″-Terpyridine-4′-thiol synthesis and standard solvents were purchased from Sigma-Aldrich. Potassium chloride (KCl) was supplied by Fluka, AZ1505 photoresist and AZ726MIF developer from Microchemicals; 3-(aminopropyl)triethoxysilane (APTES) were purchased from Alfa Aesar. Zinc (II) trifluoromethanesulfonate ($Zn(OTf)_2$) was supplied by TCI. Milli-Q grade water was used in all the experiments.

MoS2 Exfoliation: MoS_2 ink was synthesized according to the liquid phase exfoliation procedure by sonicating the bulk powders in N-Methyl-2-pyrrolidone (NMP). 80 mL of 20 mg mL^{-1} MoS_2 dispersion was sonicated for 1 h using a cuphorn sonicator (Sonics Vibra-cell VCX-750) at 60% amplitude. Then, the dispersion was centrifuged at 5500 rpm (3218 rcf) for 1 h (Hettich Mikro 220R centrifuge) and the supernatant was discarded. The precipitate was redispersed in NMP and sonicated for 6 h under the same conditions. To narrow the size and thickness distribution of the flakes, centrifugation was performed at 1000 rpm (106.4 rcf) for 90 min, followed by a second step at 2000 rpm (425 rcf) for 90 min.

Synthesis of 2,2″:6″,2″-Terpyridine-4″-Thiol (Tautomer 2,2″:6′,2″-Terpyridine-4′(1′H)-Thione, TpySH): The procedure was adapted from a previously reported synthesis (Figure S9, Supporting Information).[49] A 250 mL two-necked round bottom flask with a reflux condenser was flushed with argon and the following was added under an inert atmosphere: 4″-chloro-2,2″:6″,2″-terpyridine (0.55 g, 2.06 mmol), excess (3.50 g, 14.57 mmol) of sodium hydrosulfide hydrate and 50 mL of distilled DMF. The mixture was heated at 140 C for six hours. Then, the suspension was filtered through celite and washed 5 times with 10 mL aliquots of DMF. Afterward, the solution was transferred to the 250 mL round bottom flask and the solvent was evaporated. Obtained orange-brown solid was dissolved in ca. 10 ml of water and ammonium chloride (2.0 g, 3.13 mmol) was added to the mixture. The flask was stored in the refrigerator for 1 h and the yellow-orange precipitate was formed. The precipitate was filtered, washed with cold diethyl ether, and dried in vacuum for 48 h. Yield: 390.8 mg, 1,47 mmol, 71,7%. The solid was determined to be 2,2″:6″,2″-terpyridine-4″(1″H)-thione with >97% purity as seen by ^{1}H NMR (500 MHz, DMSO-d_6, δ): 12.30 (br s, J = 4 Hz, 1H), 8.84 (d, J = 8 Hz, 2H), δ 8.44 (d, J = 4 Hz, 2H), δ 8.05 (dt, J = 4 Hz, 2H), δ 7.62 (br t, J = 4 Hz, 2H) (Figure S10, Supporting Information).

[Zn(TpySH)2](OTf)2 Complex Synthesis: This procedure was adapted from previously reported methods.[50,51] 5–10 mg of 2,2″:6″,2‴:6‴,2⁗-terpyridine-4′-thiol was dissolved in chloroform to yield 40 mM concentration. Then, 0.5 equivalents of zinc(II) trifluoromethanesulfonate (40 mM solution in anhydrous acetonitrile) was added dropwise upon gentle stirring. Immediately, the yellow color of the TpySH solution becomes transparent, which is an indication of the formation of $[Zn(TpySH)_2](OTf)_2$ in the 4/1 v/v $CHCl_3/CH_3CN$ mixture.

Electrodes Fabrication: The electrodes were patterned on a n-doped standard Si/SiO_2 (oxide thickness: 90 nm thickness, size: 15 mm × 15 mm) by maskless photolithography (Microtech LW405B laser writer) using AZ1505 photoresist and MIF726 developer. The bottom contact channel length was L = 10 µm and width W = 10 µm (Figure S1, Supporting Information). Then, 3 nm chromium and 40 nm gold were consecutively thermally evaporated with high vacuum Plassys MEB 300 followed by a sonication-assisted lift-off process in acetone. The lift-off quality was monitored with the Olympus BX51 optical microscope.

Film Fabrication: The substrate first comprised the SiO_2 surface activation by UV/ozone treatment (NovaScan, Digital UV/Ozone System) for 20 min. Then, it was immersed in 1% APTES solution in ethanol for 30 min under mild stirring. This step is necessary to functionalize the surface with the amino group of APTES to facilitate the attachment of the MoS_2 flakes. Then, 0.5 mg mL^{-1} dispersion of 2H-MoS_2 in isopropanol was prepared and sonicated for 30 mins on an ice bath to avoid aggregation processes. The film was deposited via a step-by-step strategy using a microfluidic setup, according to a procedure developed in our laboratory. First, the silicon chip was placed in the chamber and exposed to the MoS_2 dispersion for 3 mins to create the first patches of 2D material attached to the surface. Then, the substrate was immersed in ~20 mM $[Zn(TpySH)_2](OTf)_2$ solution in 4/1 v/v $CHCl_3/CH_3CN$ mixture for 15 mins. Afterward, the chip was treated with the MoS_2 dispersion in the chamber for 10 mins and the treatment with the Zn(II) complex was repeated. The alternated depositions of MoS_2 and $[Zn(TpySH)_2](OTf)_2$ complex were repeated 5 times yielding a coverage of ≈60%. The chip was washed with IPA for 1 min and dried in N_2 stream between the steps to remove the extra material. Finally, Zn^{2+} was removed by decomplexation. The film was treated with 1 mM HCl for 15 mins and washed with MQ water. The procedure was repeated 3 times to ensure the cation removal.

Drop-Casted Film Fabrication: The procedure was adapted from Ref. [32] The MoS_2 ink was drop-casted onto IDE prepatterned Si/SiO_2 substrate and then soaked in 20 mM $[Zn(TpySH)_2](OTf)_2$ in the 4/1 v/v $CHCl_3/CH_3CN$ mixture for 24 h. Afterward, the Zn^{2+} ion was removed with 1 mM HCl treatment, that is described above.

Profilometer: To evaluate the thickness of the fabricated films, Alpha-Step IQ Surface Profiler (KLA) was employed.

Scanning Electron Microscopy (SEM): SEM images were obtained with a field emission scanning electron microscope (FEI Quanta 450 FEG), operating in high vacuum with accelerating voltages of 30 kV for the incident beam.

Raman Spectroscopy: Raman measurements were carried out with a Renishaw InVia Reflex spectrometer with high-resolution grating (2400 grooves cm^{-1}), additional band-pass filter optics, a confocal microscope, and a 2D-CCD camera. Laser excitation was performed at 532 nm with a 100× objective with 0.5% of maximum laser power for 10 seconds.

X-Ray Photoelectron Spectroscopy (XPS): The XPS spectra were collected via a Thermo Scientific K-Alpha X-ray photoelectron spectrometer with an aluminum X-ray source (energy 1.4866 keV). The X-ray spot size was settled at 400 µm. Wide-energy survey spectra were collected as an average of 10 separate scans with the pass energy of 200 eV. High-resolution spectra were collected as an average of 30 separate scans with 20 eV pass energy.

Electrical Measurements: The device response was recorded in the alternating current regime. Electrochemical impedance spectroscopy measurements were carried out using a Metrohm Autolab PGSTAT204 potentiostat/galvanostat coupled with a mini probe station (Everbeing

© 2023 The Authors. Small published by Wiley-VCH GmbH

16136829, 0, Downloaded from https://onlinelibrary.wiley.com/doi/10.1002/smll.202208100 by Library Of Trinity College, Wiley Online Library on [03/10/2023]. See the Terms and Conditions (https://onlinelibrary.wiley.com/terms-and-conditions) on Wiley Online Library for rules of use; OA articles are governed by the applicable Creative Commons License

Int'l Corp.). The impedance spectra were collected in the frequency range of 0.1 – 10^5 Hz, swept from high to low frequencies with the sine-wave voltage signal amplitude of 10 mV (root-mean-square, RMS).

Ion Sensing: All the measurements were performed in the wet state. First, the electrodes with the sensing film on top were immersed in 1 mL of the aqueous solution of $CoCl_2$/$CaCl_2$/$FeCl_3$/$MnCl_2$/KCl/$FeCl_2$/$CrCl_3$/$CuCl_2$ (concentrations ranging from 10^{-15} to 10^{-6} M) for 15 min. Then, the device was carefully rinsed with water and immersed in clean water for 5 min to remove the electrostatically attached ions. Then, the device was connected to the probe station, the rubber O-ring of appropriate size was placed on top of the chip and 100 µL of H_2O was drop-casted to keep the film wet. Each measurement was repeated 15–20 times to stabilize the signal.

Recovery Procedure: The recovery was carried out by exposing the sensors to 10 mM HCl (15 mins) under mild stirring for three times. The substrate was rinsed with water after each step.

Supporting Information

Supporting Information is available from the Wiley Online Library or from the author.

Acknowledgements

The authors thank Prof. Thomas Hermans for kindly providing the microfluidic cell and Dr. Fanny Richard for recording the XPS spectra. The authors acknowledge funding from the European Commission through the ERC projects SUPRA2DMAT (GA-833707) and FUTURE-PRINT (GA-694101), the Graphene Flagship Core 3 project (GA-881603), the Agence Nationale de la Recherche through the Interdisciplinary Thematic Institute SysChem via the IdEx Unistra (ANR-10-IDEX-0002) within the program Investissement d'Avenir, the Foundation Jean-Marie Lehn (Strasbourg) and the Institut Universitaire de France (IUF). The work carried out in Poland was financially supported by the National Science Center (grant no. 2019/35/B/ST5/01568). J.N.C. thanks Science Foundation Ireland (SFI) for support.

Conflict of Interest

The authors declare no conflict of interest.

Data Availability Statement

The data that support the findings of this study are available from the corresponding author upon reasonable request.

Keywords

defect engineering, healing point vacancies, ion sensing, selectivity, transition metal dichalcogenides

Received: December 23, 2022
Revised: March 31, 2023
Published online:

[1] L. Yu, L. Sun, Q. Zhang, Y. Zhou, J. Zhang, B. Yang, B. Xu, Q. Xu, *Biosensors* **2022**, *12*, 1096.
[2] Y. Luo, W. Guo, H. H. Ngo, L. D. Nghiem, F. I. Hai, J. Zhang, S. Liang, X. C. Wang, *Sci. Total Environ.* **2014**, *473*, 619.
[3] a) T. Goto, T. Hakuta, *Desalination* **1977**, *23*, 245; b) K. Elsaid, M. Kamil, E. T. Sayed, M. A. Abdelkareem, T. Wilberforce, A. Olabi, *Sci. Total Environ.* **2020**, *748*, 141528.
[4] H. Ali, E. Khan, *Environ. Chem. Lett.* **2018**, *16*, 903.
[5] P. D. Darbre, *Int. J. Gen Med.* **2018**, *11*, 191.
[6] J. D. Miller, M. Y. Stuckman, N. Means, C. Lopano, J. A. Hakala, *J. Chromatogr. A* **2022**, *1668*, 462924.
[7] a) C. Duran, A. Gundogdu, V. N. Bulut, M. Soylak, L. Elci, H. B. Sentürk, M. Tüfekci, *J. Hazard. Mater.* **2007**, *146*, 347; b) W. Ngeontae, W. Aeungmaitrepirom, T. Tuntulani, *Talanta* **2007**, *71*, 1075.
[8] H. Fleischer, C. Lutter, A. Büttner, W. Mittelmeier, K. Thurow, *Molecules* **2021**, *26*, 3820.
[9] Y. Lee, S.-W. Oh, S.-H. Han, *Appl. Spectrosc.* **2012**, *66*, 1385.
[10] K. Pytlakowska, *Appl. Spectrosc.* **2016**, *70*, 1891.
[11] J. Bi, T. Li, H. Ren, R. Ling, Z. Wu, W. Qin, *J. Chromatogr. A* **2019**, *1594*, 208.
[12] M. Holá, J. Kalvoda, O. Bábek, R. Brzobohatý, I. Holoubek, V. Kanický, R. Skoda, *Environ. Geol.* **2009**, *58*, 141.
[13] C. Anichini, W. Czepa, D. Pakulski, A. Aliprandi, A. Ciesielski, P. Samorì, *Chem. Soc. Rev.* **2018**, *47*, 4860.
[14] K. Leng, W. Fu, Y. Liu, M. Chhowalla, K. P. Loh, *Nat. Rev. Mater.* **2020**, *5*, 482.
[15] M. Xue, C. Mackin, W.-H. Weng, J. Zhu, Y. Luo, S.-X. L. Luo, A.-Y. Lu, M. Hempel, E. McVay, J. Kong, T. Palacios, *Nat. Commun.* **2022**, *13*, 5064.
[16] V. Montes-García, M. A. Squillaci, M. Diez-Castellnou, Q. K. Ong, F. Stellacci, P. Samorì, *Chem. Soc. Rev.* **2021**, *50*, 1269.
[17] R. Javed, M. Zia, S. Naz, S. O. Aisida, N. U. Ain, Q. Ao, *J. Nanobiotechnol.* **2020**, *18*, 172.
[18] R. Furlan de Oliveira, V. Montes-García, A. Ciesielski, P. Samorì, *Mater. Horiz.* **2021**, *8*, 2685.
[19] Y. Liu, X. Duan, H.-J. Shin, S. Park, Y. Huang, X. Duan, *Nature* **2021**, *591*, 43.
[20] C. Chang, W. Chen, Y. Chen, Y. Chen, Y. Chen, F. Ding, C. Fan, H. J. Fan, Z. Fan, C. Gong, Y. Gong, Q. He, X. Hong, S. Hu, W. Hu, W. Huang, Y. Huang, W. Ji, D. Li, L.-J. Li, Q. Li, L. Lin, C. Ling, M. Liu, N. Liu, Z. Liu, K. P. Loh, J. Ma, F. Miao, H. Peng, et al., *Acta Phys.-Chim. Sin.* **2021**, *37*, 2108017.
[21] Y. Hu, Y. Huang, C. Tan, X. Zhang, Q. Lu, M. Sindoro, X. Huang, W. Huang, L. Wang, H. Zhang, *Mater. Chem. Front.* **2017**, *1*, 24.
[22] X. Huang, C. Liu, P. Zhou, *npj 2D Mater. Appl.* **2022**, *6*, 51.
[23] V. Nicolosi, M. Chhowalla, M. G. Kanatzidis, M. S. Strano, J. N. Coleman, *Science* **2013**, *340*, 1226419.
[24] F. J. Urbanos, S. Gullace, P. Samorì, *Nanoscale* **2021**, *13*, 19682.
[25] F. J. Urbanos, S. Gullace, P. Samorì, *ACS Nano* **2022**, *16*, 11234.
[26] M. C. Lemme, D. Akinwande, C. Huyghebaert, C. Stampfer, *Nat. Commun.* **2022**, *13*, 1392.
[27] P. G. Moses, J. J. Mortensen, B. I. Lundqvist, J. K. Nørskov, *J. Chem. Phys.* **2009**, *130*, 104709.
[28] a) K. C. Knirsch, N. C. Berner, H. C. Nerl, C. S. Cucinotta, Z. Gholamvand, N. McEvoy, Z. Wang, I. Abramovic, P. Vecera, M. Halik, S. Sanvito, G. S. Duesberg, V. Nicolosi, V. F. Hauke, A. Hirsch, N. J. Coleman, C. Backes, *ACS Nano* **2015**, *9*, 6018; b) A. Stergiou, C. Stangel, R. Canton-Vitoria, R. Kitaura, N. Tagmatarchis, *Nanoscale* **2021**, *13*, 8948.
[29] S. Bertolazzi, M. Gobbi, Y. Zhao, C. Backes, P. Samorì, *Chem. Soc. Rev.* **2018**, *47*, 6845.
[30] S. Ippolito, P. Samorì, *Small Sci.* **2022**, *2*, 2100122.
[31] S. Bertolazzi, S. Bonacchi, G. Nan, A. Pershin, D. Beljonne, P. Samorì, *Adv. Mater.* **2017**, *29*, 1606760.
[32] S. Ippolito, A. G. Kelly, R. Furlan de Oliveira, M.-A. Stoeckel, D. Iglesias, A. Roy, C. Downing, Z. Bian, L. Lombardi, Y. A. Samad,

© 2023 The Authors. Small published by Wiley-VCH GmbH

16136829, 0, Downloaded from https://onlinelibrary.wiley.com/doi/10.1002/smll.202208100 by Library Of Trinity College, Wiley Online Library on [03/10/2023]. See the Terms and Conditions (https://onlinelibrary.wiley.com/terms-and-conditions) on Wiley Online Library for rules of use; OA articles are governed by the applicable Creative Commons License

V. Nicolosi, A. C. Ferrari, J. N. Coleman, P. Samorì, *Nat. Nanotechnol.* **2021**, *16*, 592.
[33] D. Tsoutsi, L. Guerrini, J. M. Hermida-Ramon, V. Giannini, L. M. Liz-Marzán, A. Wei, R. A. Alvarez-Puebla, *Nanoscale* **2013**, *5*, 5841.
[34] a) S. Okamoto, L. D. Eltis, *Metallomics* **2011**, *3*, 963; b) A. Pramanik, S. Amer, F. Grynszpan, M. Levine, *Chem. Commun.* **2020**, *56*, 12126.
[35] V. Spampinato, N. Tuccitto, S. Quici, V. Calabrese, G. Marletta, A. Torrisi, A. Licciardello, *Langmuir* **2010**, *26*, 8400.
[36] R. Saito, Y. Tatsumi, S. Huang, X. Ling, M. S. Dresselhaus, *J. Phys. Condens. Matter* **2016**, *28*, 353002.
[37] a) E. P. Randviir, C. E. Banks, *Anal. Methods* **2013**, *5*, 1098; b) H. S. Magar, R. Y. A. Hassan, A. Mulchandani, *Sensors* **2021**, *21*, 6578.
[38] V. Montes-García, R. Furlan de Oliveira, Y. Wang, A. Berezin, P. Fanjul-Bolado, M. B. González García, T. M. Hermans, D. Bonifazi, S. Casalini, P. Samorì, *Adv. Funct. Mater.* **2021**, *31*, 2008554.
[39] P. Długołęcki, P. Ogonowski, S. J. Metz, M. Saakes, K. Nijmeijer, M. Wessling, *J. Membr. Sci.* **2010**, *349*, 369.
[40] R. L. Kay, in *Aqueous Solutions of Simple Electrolytes* (Ed: F. Franks), Springer US, Boston, MA, USA **1973**, pp. 173–209.
[41] A. Stergiou, N. Tagmatarchis, *Chem. - Eur. J.* **2018**, *24*, 18246.
[42] E. Boselli, Z. Wu, A. Friedman, B. Claus Henn, I. Papautsky, *Environ. Sci. Technol.* **2021**, *55*, 7501.
[43] Y. Marcus, *Chem. Rev.* **1988**, *88*, 1475.
[44] U. S. Schubert, A. Winter, G. R. Newkome, *Terpyridine-Based Materials: For Catalytic, Optoelectronic and Life Science Applications*, Wiley-VCH, Weinheim, Germany **2011**.
[45] U. S. Schubert, H. Hofmeier, G. R. Newkome, *Modern Terpyridine Chemistry*, Wiley-VCH, Weinheim, Germany **2006**.
[46] a) K. Hoo, H. Lee, S. Choi, *J. Membr. Sci.* **2005**, *267*, 18; b) G. Türkoğlu Demirkol, S. Ö. Çelik, S. Güneş Durak, S. Acarer, E. Çetin, S. Akarçay Demir, N. Tüfekci, *Polymers* **2021**, *13*, 3201.
[47] A. K. Katz, J. P. Glusker, S. A. Beebe, C. W. Bock, *J. Am. Chem. Soc.* **1996**, *118*, 5752.
[48] M. de Lourdes Llovera-Hernández, A. Ávarez-Gallegos, J. A. Hernández, S. Silva-Martínez, *Desalin. Water Treat.* **2016**, *57*, 22809.
[49] C. W. Machan, M. Adelhardt, A. A. Sarjeant, C. L. Stern, J. Sutter, K. Meyer, C. A. Mirkin, *J. Am. Chem. Soc.* **2012**, *134*, 16921.
[50] R. Dobrawa, M. Lysetska, P. Ballester, M. Grüne, F. Würthner, *Macromolecules* **2005**, *38*, 1315.
[51] P. Huang, J. Huang, S. A. Pantovich, A. D. Carl, T. G. Fenton, C. A. Caputo, R. L. Grimm, A. I. Frenkel, G. Li, *J. Am. Chem. Soc.* **2018**, *140*, 16042.

© 2023 The Authors. Small published by Wiley-VCH GmbH

16136829, 0, Downloaded from https://onlinelibrary.wiley.com/doi/10.1002/smll.202208100 by Library Of Trinity College, Wiley Online Library on [03/10/2023]. See the Terms and Conditions (https://onlinelibrary.wiley.com/terms-and-conditions) on Wiley Online Library for rules of use; OA articles are governed by the applicable Creative Commons License